LAWRENCE
LIVERMORE
NATIONAL
LABORATORY

Sub-surface mechanical damage distributions during grinding of fused silica

T. I. Suratwala, L. L. Wong, P. E. Miller, M. D. Feit, J. A. Menapace, R. A. Steele, P. A. Davis, D. Walmer

November 30, 2005

Disclaimer

Sub-surface mechanical damage distributions during grinding of fused silica
T. Suratwala, L. Wong, P. Miller, M. D. Feit, J. Menapace, R. Steele, P. Davis, D. Walmer
Lawrence Livermore National Laboratory, P.O. Box 808, Livermore, CA 94551, USA

The distribution and characteristics of surface cracking (i.e. sub-surface damage or SSD) formed during standard grinding processes has been investigated on fused silica glass. The SSD distributions of the ground surfaces were determined by: 1) creating a shallow (18-108 μm) wedge/taper on the surface by magneto-rheological finishing; 2) exposing the SSD by HF acid etching; and 3) performing image analysis of the observed cracks from optical micrographs taken along the surface taper. The observed surface cracks are characterized as near-surface lateral and deeper trailing indent type fractures (i.e., chatter marks). The SSD depth distributions are typically described by a single exponential distribution followed by an asymptotic cutoff in depth (c_{max}). The length of the trailing indent is strongly correlated with a given process. Using established fracture indentation relationships, it is shown that only a small fraction of the abrasive particles are being mechanically loaded and causing fracture, and it is likely the larger particles in the abrasive particle size distribution that bear the higher loads. The SSD depth was observed to increase with load and with a small amount of larger contaminant particles. Using a simple brittle fracture model for grinding, the SSD depth distribution has been related to the SSD length distribution to gain insight into 'effective' size distribution of particles participating in the fracture. Both the average crack length and the surface roughness were found to scale linearly with the maximum SSD depth (c_{max}). These relationships can serve as useful rules-of-thumb for nondestructively estimating SSD depth and to identify the process that caused the SSD. In certain applications such as high intensity lasers, SSD on the glass optics can serve as a reservoir for minute amounts of impurities that absorb the high intensity laser light and lead to subsequent laser-induced surface damage. Hence a more scientific understanding of SSD formation can provide a means to establish recipes to fabricate SSD-free, laser damage resistant optical surfaces.

1. INTRODUCTION

Sub-surface mechanical damage (SSD) consists of surface micro-cracks created during grinding and/or polishing of brittle materials surfaces, such as glass. These surface cracks, often identified macroscopically as scratches and digs, are often hidden below an index-matched Bielby layer or have closed (i.e. healed); hence they are not detectable by visual inspection or standard optical microscopy until exposed by chemical etching [1]. In some use applications, the removal or minimization of SSD is required for improving the material

strength (e.g. spacecraft, underwater windows/barriers, and other military applications) where the surface flaws determine the ultimate strength or for reducing/eliminating laser-induced damage (e.g., high-peak-power laser applications [2]). For laser optic applications, SSD is believed to serve as a reservoir for absorbing precursors that will heat up and explode upon irradiation with high fluence laser light [3]. As a result, the fabrication of SSD-free optics/windows has been a goal for the optical fabrication industry for many years [4-6].

The creation of SSD can be thought of as the repeated indentation of mechanically loaded hard indentors (abrasives) sliding on the surface of an optic during various cutting, grinding and polishing processes. The initiation and growth of the three basic types of cracks (lateral, radial, Hertzian) resulting from a single, static indentor as a function of load, material properties of the indentor and substrate are known (see Fig. 1 and Discussion in Sec. 4.1) [7-8]. These relationships have served as the basis for estimating material removal during grinding of brittle materials [9, 7, 10]. Others have utilized these basic fracture relationships, combined with experimental data, to relate the SSD depth to basic processing parameters such as load, abrasive size and the resulting surface roughness [11, 12, 13]. Preston was among the first to recognize the presence of SSD on finished surfaces and that etching exposes the chatter mark cracks (which we will refer to as trailing indent fractures) [14]. Since then, a wide variety of destructive and non-destructive techniques for measuring the amount and depth of the SSD have been explored [13, 15-19]. Some of the more direct SSD measurement techniques include the ball-dimple method [20], taper polishing method [21], and more recently a MRF spot method [22], where the ground or finished surface is partially removed to evaluate the depth of the SSD.

In the following study, we use a taper polishing method, where various ground fused silica surfaces are subsequently treated by an an advanced finishing technique (magneto-rheological finishing or MRF), known not to induce SSD, to create a shallow surface taper over relatively large areas to determine the statistical distribution of SSD [23, 24]. We then apply known indentation fracture and wear relationships [7, 8, 4] to establish insights into the nature of the cracking, the load per particle present, the shape of the distributions, and the maximum SSD depth. Such a data set combined with fracture mechanic insight serves as a means to understand and to predict a SSD distribution for a given grinding/polishing process and to serve as useful tool for performing and designing optical fabrication processes.

2. EXPERIMENTAL

2.1 Sample Surface Preparation

Twelve round fused silica glass (Corning 7980) samples (10 cm diameter × 1.0 cm thick) labeled as Samples A-L were ground & polished such that they contained minimal subsurface damage. One face of each sample was then treated by one of several standard grinding processes. **Sample A (Sandblasted)** was sand blasted (Zero Blast-n-Peen Model NPGS-4) using 300 μm Al_2O_3 abrasive for 15 min. **Sample B (120 grit Coarse Blanchard)** was generator ground on a Blanchard Model 11A20 using a 120 grit (125 μm) diamond in metal matrix tool (downward feed rate = 250 μm/min, rotation rate = 45 rpm, time= 20 sec). **Sample C (150 grit Coarse Blanchard)** was generator ground on a Blanchard Model 11 using a 150 grit (100 μm) diamond in resin matrix tool (downward feed rate = 230 μm/min, rotation rate = 41 rpm, time= 20 sec). **Sample D (15 μm Loose Abrasive)** was ground on a Strasbaugh

Model 6Y2 grinder using 15 μm Al_2O_3 abrasive (Microgrit WCA15T) in water on a Pyrex glass lap (load = 25 N, lap rotation rate = 16 rpm, time= 1 hr). **Sample E (15 μm Fixed Abrasive)** was ground on a Strasbaugh (Model 6DA-DC-2) using 15-μm diamond fixed abrasive in an epoxy matrix (Gator Diamond) (load = 25 N, lap rotation rate = 16 rpm, time= 1 hr). **Sample F (9 μm loose Abrasive)** was ground on a Strasbaugh Model 6Y2 grinder using 9 μm Al_2O_3 abrasive (Microgrit WCA9T) in water on a Pyrex lap (load = 25 N, lap rotation rate = 36 rpm, time= 1 hr). **Sample G (7 μm Fixed Abrasive)** was ground on a Strasbaugh Model 6DA-DC-2 grinder using 7 μm diamond fixed abrasive in an epoxy matrix (Gator Diamond) (load = 25 N, lap rotation rate = 16 rpm, time= 1 hr). Samples H-L were prepared as variations or sequences of the treated samples described above, which are described in more detail in the results section. The surface roughness for each of the treated surfaces was measured by a contact stylus profilometer (KLA Tencor P-10 surface profiler). Scans were made on four random areas of 5 mm length on each the samples; no filtering was performed. The calculation of the roughness is described in Sect. 4.5.

2.2 SSD damage measurement

Figure 2 shows a schematic of the process used to measure the SSD distribution for a given surface. The details of this process are outlined elsewhere [23] and are briefly described here. Each treated sample was: (1) polished by a MRF (which is known to cause little or no surface damage) to create a precise, shallow, linear wedge (over a 6.5 cm square patch) having a maximum depth ranging from 18-108 μm depending on the sample; 2) etched in 20:1 BOE (buffered oxide etch) for ~20 min to expose the cracks on the surface; 3) documented by bright field transmission optical microscopy (Nikon Optiphot 300) at 75x and 300x magnification at various distances along the surface wedge; and 4) analyzed by image analysis (using ImageJ software) to determine the length and depth distribution of cracks. Image analysis was performed by first thresholding the microscope images to create binary renderings such that the cracks on the surface are dark pixels and the background is white. For the crack depth distribution data, the total obscuration (fraction of the area that is composed of cracks) was calculated at various distances along the wedge (i.e. depth into the original sample surface). Multiple images were often utilized in the analysis at a given length along the wedge when the number of observed crack features was low to establish better statistics (i.e. to reduce the error bar). For the crack length distribution, the obscuration of each of the individual, isolated cracks (not cracks that intersected each other) was determined. The crack length distribution was then calculated by dividing the obscuration of each crack by the average crack width. The crack width is only a function of the etch time, and hence constant for a given sample. Also, the crack length distribution was found to be independent of the crack depth or distance along the wedge; hence the lengths of the isolated cracks were calculated at all depths along the wedge. Between 300 and 12000 cracks were charactered for each sample to obtain the crack length distributions.

The error in the obscuration was calculated by repeatedly measuring (3-5 times) a single sample at different locations and determining the repeatability of the obscuration measurement. The variability in the data is different for different obscuration ranges, since the measured obscuration often spans six orders of magnitude. At high obscurations (0.1-1), the repeatability is ±2%; at medium obscurations (10^{-2}-10^{-3}), it is ±25%; and at low obscurations (10^{-4}-10^{-6}), it is ±125%. The error in the measured depth is governed by the range of depths

observed in a single image and the slope of the wedge, as-prepared. Most of the analysis was performed at 75x which had a field of view of 1.78 mm. For shallow wedges (18 μm), the depth range is ±0.3 μm; for medium wedges (50 mm), it is ±0.7 μm; and for deeper wedges (108 mm), it is ±1.6 μm. Note that no obscuration data was collected in the first two microns of depth, because slices that thin on the wedge were not created.

2.3 Measurement of fused silica indentation parameters

On a separate polished fused silica surface, a series of Vickers (sharp) indents were applied on fused silica at different loads ranging from 0.1 N – 20 N. Also, a series of Brinell indents (radius 1 mm) were applied on fused silica at different loads ranging from 15 N – 130 N. The indents were prepared using a standard Zwick Model T3212 hardness tester. The sample was then etched in buffered oxide etch (BOE) (20:1) for 20 minutes. The depths of the radial crack from the Vickers indent were determined as half of the average of the two radial crack diameters visible on the surface. The depths of the lateral cracks from the Vickers indents were determined by the change in focus from the substrate surface to bottom plane of the lateral fracture. The size of the Hertzian cone fractures (c_h) were calculated from the vertical depth of cone fractures into the surface by change in focus in the microscope, the contact zone diameter, and the diameter of the cone fracture at its deepest point in surface. The Hertzian cone depths and the Vickers lateral crack measurements were corrected by the glass' refractive index of 1.46.

3.   RESULTS

3.1 Microscopy of the surfaces
Table 1 summarizes the experimental parameters and results for the 12 ground samples measured in this study. Figures 3 and 4 show a selected series of microscope images for each sample at various distances along the produced surface wedge (i.e., depths below the original ground surface) after etching. The crack features observed were typically visible by optical microscopy only after BOE etching. The crack number density at the ground sample surface was very high, such that the individual cracks intersect many other cracks. This rubble-like appearance (not shown in Fig.) makes it difficult to categorize the crack type. However, a few microns below the surface (i.e. after polishing through the surface layer), one can now identify distinct individual cracks all of a common morphology which decrease in number density with depth. For the most part, these cracks have a 'trailing indent' character (commonly referred to as chatter marks [1,7] or stick-dig fractures). Figure 5a shows a schematic of the geometry of an individual trailing indent crack and Fig. 5b shows a microscope image of a series of trailing indent cracks caused by scratching a glass surface. The crack depth (c) is the depth of an individual trailing indent crack into the surface; crack length (L) is the longer dimension of the crack as viewed on the sample surface in the microscope; and crack width (w) is the shorter dimension of the crack as viewed on the sample surface in the microscope image. Further examination of Figs. 3 and 4 reveal that there is a characteristic crack length associated with each sample which scales roughly with the size of the abrasive used to grind that surface. This characteristic crack length does not generally change with depth for a given sample.

3.2 Crack depth and length distributions

Figures 6 and 7 show the measured crack depth and length distributions for each of the samples. The crack depth distributions are reported in terms of cumulative crack obscuration (crack area fraction) as function of depth into the original treated glass surface. Obscuration was used instead of crack number density as the units to describe the SSD density because the intersection of cracks near the surface caused significant uncertainty in the number density count of the cracking. The shape of the depth distributions follow single exponential dependence for the majority of the distribution except near the end of the distribution where crack density drops very rapidly appearing like an asymptotic cutoff. In some cases, the exponential dependence spans 4-5 orders-of-magnitude (see Fig. 6a). Also, the overall depth of SSD generally increases with increase in the abrasive size of the grinding process (Fig. 6a). The crack length distributions are plotted in terms of cumulative number distribution as a function of crack length. For these distributions, only discrete cracks (non-intersecting cracks) were counted. Again, the mean crack length for each grinding process generally increases with increase in abrasive size (see Table 2).

3.3 Indentation parameters for fused silica

Table 2 shows the measured indentation crack depths for Hertzian (c_h), radial (c_r), and lateral cracks (c_ℓ) as a function of various indentation loads during Brinell or Vickers indentation. For all crack types, once initiated, the size of the crack increased with load. The initiation load was very different for the three different crack types.

4. DISCUSSION

4.1 Relationships governing SSD crack formation

Grinding of glass can be described by brittle fractures caused by an ensemble of normally-loaded, hard-indentors (abrasives) sliding/rolling across the surface of the glass workpiece. The brittle fracture will lead to both material removal and development of SSD. There are three basic types of fractures that can occur by static indentation: 1) Hertzian cracks [7], 2) radial cracks [7,9], and 3) lateral cracks [7,9] (see Fig. 1). Hertzian cracks are cone cracks that are created from a spherical indenter; radial cracks are semi-circular cracks perpendicular to the glass surface from a sharp indenter; and lateral cracks are cracks that run generally parallel to the glass surface which are also typically created by a sharp indentor. By their geometry, it is clear that formation of lateral cracks will largely lead to material removal and will contribute significantly to the observed surface roughness. Hertzian and radial cracks, on the other hand, will largely contribute to deeper SSD and potentially to some material removal through the intersection with other cracks. The relationships that govern the initiation load (P_c) to first observed fracture on the surface have previously been described as [7,9]:

$$P_{ch} = A\,r \tag{1a}$$

$$P_{cr} = \alpha_r \frac{K_{Ic}^{\,4}}{H^{\,3}} \tag{1b}$$

$$P_{c\ell} = \text{constant} \tag{1c}$$

where A is Auerbach's constant (N/m), r is the local indenting radius of curvature (m) , K_{Ic} is the glass fracture toughness (MPa•m$^{1/2}$) and H is the glass hardness (GPa). The subscripts h, r, ℓ are designations for Hertzian, radial and lateral cracks, respectively. The initiation load for the radial crack is described in terms of the index-of-brittleness previously described by Lawn et. al.[7]. For a constant contact radius (a) with decreasing r of the particle, the 'sharpness' of the particle increases. As r approaches zero, then the stress at the contact point approaches infinity. Physically, when the stress approaches the yield stress, irreversible plastic deformation occurs beneath the indentor on the workpiece until it can support the load.

The relationships that govern the depth of the fractures (c) generated after initiation are given by [7,9]:

$$c_h = \left(\frac{\chi_h P}{K_{Ic}} \right)^{2/3} \tag{2a}$$

$$c_r = \left(\frac{\chi_r P}{K_{Ic}} \right)^{2/3} \tag{2b}$$

$$c_\ell = \frac{\chi_\ell \left(\dfrac{E}{H} \right)^{2/5} P^{1/2}}{H^{1/2}} \tag{2c}$$

Where χ is the growth constant (unitless), E is the elastic modulus for the glass (GPa), P is the applied normal load per particle (N). The crack depths for Hertzian and radial cracks scale as $P^{2/3}$, and the crack depth for lateral cracks scales as $P^{1/2}$.

The above description assumes a static indent (i.e. a non-moving particle on a frictionless interface). When considering grinding processes, sliding/rolling must be taken into account and friction between the particle and the glass surface becomes important. For a sliding sphere, which has been analyzed by Lawn et. al. [25], the movement leads to a change in the stress distribution such that the peak tensile stress is at the trailing edge of the particle. Fracture at the surface will now have the shape of an arc as opposed to a circular ring fracture commonly observed with frictionless Hertzian cone contact [11, 25]. These chatter, slip-dig or partial cone type fractures are referred to as trailing indent fractures in this study (see Fig. 5b). The 'trailing indent' initiation load (P_{ct}), the crack depth (c_t) and the crack length (L_t) for a spherical particle are given by [25]:

$$P_{ct} = \frac{A r}{(1 + B\mu)^2} \tag{3a}$$

$$c_t = \left(\frac{\chi_h (1+\mu^2)^2 P}{K_{Ic}} \right)^{2/3} \tag{3b}$$

$$L_t \cong \frac{1}{4} \pi (2a) \cong \frac{\pi}{2} \left(\frac{2}{3} \frac{k}{E} P d \right)^{\frac{1}{3}} \tag{3c}$$

where B is a friction constant (unitless) , μ is the friction coefficient (unitless), a is the contact radius for a Hertzian contact (m), d is the 'effective' abrasive diameter assuming a spherical particle (m), and k is a ratio of material constants given by:

$$k = \frac{(1-\nu_p{}^2)}{E_p} + \frac{(1-\nu^2)}{E} \qquad \textbf{(4)}$$

where ν & ν_p are the Poisson's ratio for the workpiece glass and the indentor abrasive particle, respectively. E and E_p are the Young's modulus of the workpiece glass and indentor particle, respectively. As the friction coefficient goes to zero, the expression become identical to the Hertzian initiation and growth relationship described earlier (1a & 2a). The frictional forces significantly reduce the initiation load (P_{ct}) for a trailing indent crack compared to frictionless Hertzian crack. However, the growth of a trailing indent is slightly increased with increase in friction compared to a frictionless Hertzian crack [25]. The crack length of trailing indent fracture is simply approximated as ¼ of the Hertzian contact circumference.

Figure 8a plots the depths of the lateral cracks as a function of $P^{1/2}$, and Fig. 8b plots the depth of the Hertzian cracks and radial cracks as a function of $P^{2/3}$, respectively, as a function of load for the cracks that were created by standard Vickers and Hertzian indentation. A reasonable linear fit is obtained for all three sets of data, suggesting that the observed load dependence is consistent with the indentation growth expressions shown in Eqs. 2a-2c. The x-intercept values from the linear fits were used to calculate α_r & A using equations 1a-1b and to determine $P_{c\ell}$. The slopes of the linear fits were used to calculate χ_ℓ, χ_r, and χ_h using Eq. 2a-2c. These determined values are listed in Table 2 and compared with some literature values.

4.2 Fraction of abrasive particles being mechanically loaded

The indentation fracture relationships described in Section 4.1 can be used to illustrate that the fraction of abrasive particles being loaded and leading to fracture is quite small. Take, for example, Sample H (9 µm loose abrasive), and assume: 1) all the abrasive particles between the lap and the workpiece are evenly mechanically loaded; and 2) the fill fraction of particles below the work piece is ~0.3 [26]. Since the friction coefficient is not known and since its effect on crack depth is small (see Eq. 3b), Eq. 2a is used to estimate the depth of damage for a 'trailing indent' crack. For a 10-cm-diameter workpiece and a 9-µm-diameter abrasive, the total number of particles below the workpiece (N_T) [the surface area of the workpiece times the fill fraction (f) divided by the surface area of the particles below the workpiece] is 10^8. Given a total load (P_T) of 25 N, the load per particle ($P=P_T/N_T$) is then $2 \cdot 10^{-7}$ N. Substitution of the values from Table 3 into Eq. 2a, a crack depth of only 3.5 Å is calculated! This prediction is ~10^4 smaller than the measured value of c_{max} (6 µm). A reasonable explanation for this discrepancy is that only a small fraction of the particles are being loaded.

The fraction of particles being loaded for given fracture depth ($f_L(c)$) can be described as:

$$f_{load}(c) = \frac{N_L}{N_T} = \frac{\chi_h P_T}{K_{Ic} c^{3/2}} \cdot \frac{d_c{}^2}{f \, d_{optic}{}^2} \qquad \textbf{(5)}$$

where N_L is the number of particles being loaded to get a SSD depth of c. Using Eq. 5, $f_{load}(c)$ is plotted for all the samples in which the P_T (the total load) is known (i.e. all the samples except the sandblast and the generator grind samples) (see Fig. 9). The plots are shown for SSD depths ranging from 0.5 µm to c_{max} for each of the samples. At shallow SSD depths (say

1 μm) the fraction of the particles being loaded to cause that damage is calculated as 10^{-3} to 10^{-5}. At SSD depths approaching c_{max}, the fraction of the particles is 10^{-5} to 10^{-7}. In other words, to cause the deepest SSD only 1 out of 100,000 to 10 million particles is being loaded to cause the fracture! Others have come to similar conclusions regarding the load bearing particles [27-28].

It is likely that the larger particles in the tail end of the abrasive particle distribution are the load bearing particles. Figure 10 shows the abrasive size distribution of the 15 μm loose abrasive (Microgrit 15T) provided by the manufacturer fit to a log-normal distribution. By extrapolating the size distribution data with the log-normal fit and using Eq. 5, a rough estimate of the size of particles being loaded can be obtained (22-28 μm). Note that this calculation is very sensitive to the function used to fit the tail end of the distribution; the values obtained should be used with caution. However, this analysis does qualitatively give an impression of the sizes of particles being loaded, relative to the mean abrasive size.

4.3 SSD depth distribution shape as a function of material removal

Two major factors that determine the <u>shape</u> of the SSD depth distribution are: 1) the fundamental instantaneous distribution of cracks ($f_o(c)$) generated at some time and 2) the summation of the fundamental distribution of cracks and their continued shortening with continued time and material removal. A simple model is utilized to evaluate relationships between $f_o(c)$ and the final observed SSD depth distribution ($F_c(c)$).

Assume at some time (t) or amount of material removed (Δ), a distribution of cracks is generated ($f_o(c)$) (see Fig 11a). In removal increments of Δ, another set of cracks of the same distribution are created but starting at the new surface of depth $i \cdot \Delta$, where i is the number of increments. For this model, previously generated cracks are assumed not to grow. In addition, previously generated cracks are continually made shorter and eventually removed with each removal, resulting in a new total incremental distribution of cracks given by:

$$f_c(c) = f_o(c) + f_o(c+\Delta) + f_o(c+2\Delta)... = \sum_i f_o(c+i\Delta). \qquad (6)$$

The cumulative distribution of crack depths is then simply:

$$F_c(c) = \int_c^\infty f_c(c) \, dc. \qquad (7)$$

For the present discussion we will assume that $f_o(c)$ is a Gaussian distribution. The fundamental crack distributions for different removal increments of Δ are illustrated in Fig. 11b. Fig. 11c shows the resulting $F_c(c)$ & $f_c(c)$ distributions using Eqs. 6 & 7 on a semi-log plot for a large value of n (i.e. at steady-state where the rate of crack generation equals the rate of crack removal). The cumulative crack distribution $F_c(c)$ is representative of the measured SSD depth distribution shown in Fig. 6a. The summing of $f_o(c)$ to get $f_c(c)$ results in a linear profile except at the ends of the distribution. This linear profile would result regardless of the functional form of $f_o(c)$. However, near the end of the distribution at low obscuration (i.e. the deepest cracks), the shape of the distribution $F_c(c)$ tends to have the same basic shape or functional form of $f_c(c)$ and $f_o(c)$ (see Fig. 6c).

This fundamental distribution of cracks ($f_o(c)$) is likely governed by the particle size distribution of the abrasive and the load/particle (see Section 4.4). Hence, since the measured data follows a single exponential, $f_o(c)$ and the particles participating in fracture distribution is also expected to be a single exponential. This simple model implies that the deepest cracks in

the distribution are created in the last increments (i.e. the end of grinding process). Another interesting result from this simple model is that shape of the tail end of the calculated distribution appears as a single exponential using a Gaussian distribution for $f_o(c)$, which matches the shape of the observed SSD distribution shown in Figs. 6 & 7. An exponential dependence of the SSD distribution is also obtained using various types of fundamental distributions of cracks such as log-normal and Lorentzian.

4.4 Relationship between the crack length distribution and crack depth distribution

Because cracks are not all the same depth, it is clear that the load for a given particle varies. It is sensible to assume that the larger abrasive particles bear a larger load (see Section 4.2). Hence, the particle size distribution of the abrasive is related to the fundamental crack distribution ($f_o(c)$). This relationship, however, is complicated by many factors such as: 1) only the tail end (largest particles) of the distribution is participating in the fracture event; 2) agglomeration, comminution, rotating particles, and the addition of foreign particles can occur; 3) the ability of loaded particles to initiate fractures can change with pre-existing fractures present on the surface (i.e. change in the stress profile or stress intensity at the crack tip); and 4) the roughness of the lap and workpiece as well as the overall interface gap can alter the load/particle. Without knowing the effects of each of these complicating factors, the measured crack length distribution can be related to measured crack depth distribution to determine an 'effective' particle size distribution (d) participating in fracture. This 'effective' size distribution can then be potentially benchmarked to the real particle size distribution as means to estimate damage caused by different processes.

For this analysis or engineering model, all the observed cracks leading to SSD are assumed to be trailing indent fractures with the geometry outlined in Fig. 5a, and their crack growth will be approximated using the Hertzian crack growth relationships (friction=0). The cracks near the surface (such as lateral cracks) are ignored. For simplicity, we will assume that the surface of the lap and the workpiece are smooth and flat, and the gap (x) is fixed and not time varying. The particles are all assumed to be spherical. Also, we will assume that loading time and rate effect are not important; in other words, the lap and workpiece are treated as purely elastic materials. The load/particle is assumed to be proportional to the depth of penetration of the particle in the lap or the workpiece. In other words for a fixed gap (x), it is the vertical dimension of the particle, which for spherical particles is just the 'effective' particle size (d), that is directly proportional to load (see Fig. 12). The linear dependence of load with particle size has also been used in other grinding models [3, 27, 28]. The load for a given 'effective' particle size (d) is then defined as:

$$P(d) = \frac{P_T}{N_L}\left(\frac{d}{d_c}\right) \tag{8}$$

where P_T is the total applied load on the part, N_L is the number of particles being loaded on the workpiece, and d_c is the mean particle size of the used abrasive. Then by substitution of Eqs. 2a, 3c, and 8, the 'effective' spherical particle size for a given crack length is determined as:

$$d(L) = L^{3/2}\left(\frac{2}{\pi}\right)^{3/2}\left(\frac{3EN_L d_c}{2kP_T}\right)^{1/2} \tag{9}$$

and the crack depth for a given crack length is determined as:

$$c = \frac{L}{\Omega} \tag{10}$$

where,

$$\Omega = \frac{\pi}{2} \left(\frac{K_{Ic}}{\chi_h} \right)^{2/3} \left(\frac{2k\,Nd_c}{3E\,P_T} \right)^{1/3}. \tag{11}$$

Eq. 10 suggests that the crack length is linearly related to crack depth for a constant Ω. Hence deeper cracks will have longer crack lengths.

As a means to test the above formalism, the measured crack length distribution will be used to describe the crack depth distribution. First, the process of converting from cumulative crack length distribution ($F_L(L)$) (Fig. 6b) to cumulative crack depth distribution in terms of obscuration ($O(c)$) (Fig. 6a) will be described generically. From $F_L(L)$ it is straight forward to obtain the fractional crack length distribution ($f_L(L)$) as:

$$f_L(L) = \frac{\partial F_L(L)}{\partial L} \tag{12}$$

which is simply a description of the fraction of cracks with lengths within a crack length range of ∂L. The fractional 'effective' particle size distribution ($f_d(d)$) and fractional crack depth distribution ($f_c(c)$) can be determined:

$$f_d(d) = f_L(L) \frac{\partial L}{\partial d} \tag{13}$$

and

$$f_c(c) = f_d(d) \frac{\partial d}{\partial c}. \tag{14}$$

The fractional crack depth distribution ($f_c(c)$) will have units of #/area; however the measured depth distribution is in terms of obscuration. The fractional crack depth distribution in terms of obscuration ($o(c)$) can be then described as:

$$o(c) = f_c(c)\, w\, n\, L(c) \tag{15}$$

where w is the width of the crack (μm), n is the surface crack density (cm^{-2}), and $L(c)$ is the crack length as a function of crack depth which can be obtained from simply rearranging Eqs. 10 and 11. The measured SSD depth distribution is a cumulative distribution in units of obscuration or crack area fraction, which is given by:

$$O(c) = \int_c^{c_{max}} o(c)\,dc \tag{16}$$

The cumulative nature of the measured depth distribution arises because the microscope images are taken of a given surface shows all the cracks at that depth and deeper into the surface.

The process described above for converting from $F_L(L)$ to $O(c)$, is shown in generic form and makes no assumption of the functional form of the $F_L(L)$. We find that $F_L(L)$ fits well to the data using a single exponential (see Fig. 6b) in the form of:

$$F_L(L) = 1 - A \exp\left(\frac{-L}{\langle L \rangle} \right) \tag{17}$$

where A is constant and <L> is the mean crack length (see Table 1 for values). Eq. 7 is bound between $L=L_{min}$ and $L=L_{max}$. L_{min} is the minimum detectable crack size for the microscope images taken ($L_{min}= 2$ μm for all samples except sample F for which $L_{min}=0.5$ μm because

images were taken at higher magnification). L_{max} was determined from the data plotted in Fig. 6b and its values are reported in Table 1. Note, as discussed in the previous section, that the average crack length ($<L>$) is unique for each given grinding process. By assuming this functional form for $F_L(L)$ (Eq. 17) and performing the conversion to O(c) described above, the resulting form of the SSD crack depth distribution in terms of the crack length distribution parameters is then:

$$O(c) = A \, w \, n \, \Omega \left(c + \frac{\langle L \rangle}{\Omega} \right) \exp\left(\frac{-c \, \Omega}{\langle L \rangle} \right) - $$
$$A \, w \, n \left(L_{max} + \langle L \rangle \right) \exp\left(\frac{-L_{max}}{\langle L \rangle} \right)$$
(18)

where the first term describes the initial depth distribution, which is roughly a single exponential, and the second term is a constant related to the maximum depth of the SSD (c_{max}). c_{max} can also be calculated directly as:

$$c_{max} = \frac{L_{max}}{\Omega}.$$
(19)

To check the consistency of the above formalism, we fit the measured SSD depth distribution using Eq. 18. The following values were used as known parameters: k=0.65, E=72.7 GPa, χ_h=0.034, K_{Ic}=0.75 MPa m$^{1/2}$, w (see Table 1), d_c (see Table 1), A (see Table 1), and $<L>$ (see Table 1). L_{max} is also a known measured parameter, but will be used as a fitting parameter and then compared to the measured results. The two remaining parameters, P_T/N_L (average load per loaded particle) and n (number density of cracks on the surface) were used as the fitting parameters for each sample. The best-fit values for these parameters for samples A-G and K-L are shown in Table 1 and plotted in Figs. 6a and b. Except for the 9-μm loose abrasive (Sample F), the values for n ranged from 2.5-40 x 10^5 cm^{-2} and the values for P_T/N_L ranged from 6-1400 $\times$ 10^{-4} N. Also, the average load per loaded particle generally increased and the number density of surface cracks generally decreased with increase in abrasive size; both are trends that would be expected. A similar exercise was performed for Samples H, I and J as described above. However, the crack length distribution fit better to a double exponential. The results for these samples are also summarized in Table 1.

Using the engineering model described above, the 'effective' particle size distribution participating in fracture can be calculated. Substituting Eqs. 17, into 12 and 13, we get:

$$F_d(d) = \frac{A}{\langle d \rangle} \exp\left(\frac{-d}{\langle d \rangle} \right)$$
(20a)

where $<d>$ is the mean abrasive size participating in the fracture:

$$\langle d \rangle = \langle L \rangle^{3/2} \left(\frac{2}{\pi} \right)^{3/2} \left(\frac{3 E N_L d_c}{2 k P_T} \right)^{1/2}$$
(20b)

The calculated 'effective' particle size distribution is shown in Fig. 13 and the calculated values for $<d>$ are listed in Table 1. Except for the sandblast (Sample A) and the 7-μm fixed abrasive (Sample G), $<d>$ was found to scale linearly with the mean abrasive size with a ratio of ~10-11 (see Table 1). This relationship may serve as a connection between process parameters and SSD.

Remember, the 'effective' size distribution differs from the real abrasive size because of all the factors listed in the beginning of this section. Also, the 'effective' size distribution

assumes all the particles are spherical. In fact, most abrasives are not spherical, but more oblate (plate-like). Hence, the size of the particle is related to the radius of curvature by some shape factor s (i.e. d = s2r). For spherical particles s=1 and for particles more plate-like s<1.

Figure 14 is a plot comparing L_{max} (measured) and L_{max} (fit) used to determine the best fit of Eq. 18 to measured depth distribution data. The measured L_{max} deviated from the fit value of L_{max} where fit L_{max} was noticeably higher; however there was a linear relationship between the two. Our measurement of L_{max} is dependent on the quantity of cracks evaluated and hence is not a robust value; L_{max} (measured) was typically calculated from a data set of 300-12000 cracks. However, L_{max} (fit) is related to c_{max} which occurs at obscuration levels of 10^{-6} or one out of a million cracks. The difference between the measured L_{max} and the fit L_{max} maybe just due to the fact that not enough cracks were characterized.

4.5 Relationship of roughness and average crack length to the maximum SSD depth

Figure 15a is a plot which shows a linear correlation between maximum SSD depth (c_{max}) and surface roughness (δ) with a proportionality constant (k_{max}) of 49. The values of k_{max} have been measured by others for fused silica and other glasses: Preston (~3) [14]; Aleinkov (~4) [13]; Lambropoulos (<2) [19, 30]; Randi (1.4) [22] and P. Hed (5-8) [21]. This proportionality between SSD and roughness is often used by opticians to estimate the amount of SSD for a given grinding process using the measured roughness. However, it is difficult to compare results, since the value of the measured roughness is subject to large variations depending on the method of measurement (e.g. profilometry vs white light interferometry), the spatial range measured, the length of the surface or area measured, and the calculation method. Most [19; 22; 21] have found that the peak-to-valley roughness (δ_{PV}) (the highest height minus the deepest valley) as opposed to average or rms roughness [29] provides the best correlation to SSD depth. However, the (δ_{PV}) measurement is very sensitive to the length of the scan and the position of the surface measured. Our measurements of δ_{PV} often range $\pm40\%$ upon repeated measurements of the same sample. One method to calculate a roughness that is more repeatable and still emphasize the higher amplitude features on the surface is to use:

$$\delta = \left(\frac{1}{L} \int_0^L y(x)^n dx \right)^{1/n} \tag{22}$$

where y(x) is the surface topology (y is the height/amplitude and x is the distance along surface). For larger values of n, the value of δ emphasizes the higher amplitude features. When n=2, the δ is the same as the root-mean-square (rms) roughness. Using n=4, emphasized the higher amplitude features as well as reduced the repeatability error to $\pm12\%$; this measure of roughness also leads to a good correlation with SSD depth (see Fig. 15a).

The relationship between surface roughness and SSD depth can be thought of in terms of the relationship between lateral crack depth and trailing indent crack depth (see Fig. 16) [30]. The higher amplitude features on the surface can be thought of as isolated lateral cracks. Assuming the surface roughness (δ) (calculated using Eq. 22) is equal to the lateral crack depth (c_ℓ), the proportionality constant (k_{max}) using Eq. 2c is then:

$$k_{max} = \frac{c_{max}}{\delta} = \frac{c_{max}}{c_\ell} = \frac{c_{max}}{\dfrac{\chi_\ell \left(E/H\right)^{2/5}\left(P_T/N_L\right)^{1/2}}{H^{1/2}}} \qquad \textbf{(23)}$$

Substituting in values for P_T/N_L from Table 1, we get k_{max} values ranging from 25-39; the measured value of k_{max} was 49.

Figure 15b is a plot showing the correlation of the average crack depth ($<c>$) and the maximum SSD depth (c_{max}) with mean crack length ($<L>$). Both measures of SSD depth correlate linearly with the mean crack length, as predicted by Eq. 10 assuming Ω is fairly constant. The values of Ω were essentially constant (values between 3-5) for Samples A-G. The relationship between crack length and crack depth has some important practical consequences. Upon measuring the length of a crack on a work-piece, one can estimate its depth. According to Fig. 15b, on average, the crack depth will be 37% of the length; however the crack could be as deep as 2.8 times the crack length.

4.6 Effect of load, particle contamination, and crack growth

Figures 7a & d show the crack depth and length distributions, respectively, of a series of 9 μm loose abrasive grinding processes performed at three different loads (25 N, 220 N, 580 N). With an increase in load, the crack depth and crack length increased. Also, with an increase in load, a second kink in the SSD depth distribution appears which was not observed at the lower load. This suggests a second distribution of particles are being loaded and causing fracture at the higher loads.

Figures 7b & e show the crack depth and length distributions for the 9 μm loose abrasive (Sample F), 15 μm loose abrasive (Sample D), and 9 μm loose abrasive contaminated with 0.1 wt% of the 15 μm loose abrasive (Sample J). The SSD depth increased significantly with the addition of this contaminant. Interestingly, a small amount of contaminant in Sample D led to deeper SSD than just using the 15 μm loose abrasive alone (Sample D). This suggests that the load/particle for fewer larger particles is high relative to Sample D.

Figures 7c and f show the crack depth and length distributions for generator and samples: 120 grit (Sample B), 150 grit (Sample C), 120 grit followed by the 150 grit (Sample K), and 120 grit, etching, then followed by the 150 grit (Sample L). The intention of this series of samples was to determine if cracks from a previous process would grow and change the SSD depth distribution with respect to performing only the last step in the process. Also, if they do grow, does blunting the cracks by etching affect the ability of these cracks to grow? For Samples K and L, ~100 μm of material was removed during the 150 grit generator process to ensure that the removal was greater than the SSD damage caused by the 120 grit generator process. By examining Fig. 7c, Samples K & L did not show any significant difference in the SSD depth distributions compared to Sample C. This suggests, to first order, that cracks that preexisted in the 120 grit process did not grow any deeper than the cracks that are caused by the 150 grit process alone.

5. CONCLUSIONS

The SSD depth and length distributions for various grinding processes have been directly measured and statistically evaluated. The observed surface cracks are characterized as near-

surface lateral and deeper trailing indent type (i.e., chatter marks) fractures. The length of the trailing indent is strongly correlated with a given process. The SSD distributions are typically described by a single exponential distribution followed by an asymptotic cutoff in depth (c_{max}). Using fracture indentation relationships, it is shown that only a small fraction of the abrasive particles are being loaded and participating in the fracture, and it is the larger particles in the abrasive particle size distribution that bear the higher loads. Using a mechanical model to describe the grinding process, the measured crack length distribution has been related to the crack depth distribution. This correlation, has also allowed for estimating the 'effective' particle size distribution participating in fracture, whose particle sizes are ~10 times the mean abrasive particle size. The maximum SSD depth was found to correlate with both the mean crack length and the measured surface roughness. The ratio of c_{max}/δ was found to be 49. Also, the observed relationship between the mean crack length and the maximum SSD depth, can be utilized as a rule-of-thumb to non-destructively estimate the depth of SSD by measuring the crack length of an individual SSD defect. For grinding performed in sequence, the SSD depth distribution did not noticeably influence the SSD caused from the previous grinding step provided that material removal exceeded the SSD depth of the previous step. A small amount of contaminant of larger abrasive particles can greatly increase the SSD depth, even more so than just using only the contaminant, because the load/particle is higher.

5. ACKNOWLEDGEMENTS

REFERENCES

1) G. Beilby, Aggregation and Flow of Solids, 1st Ed, London: Macmillan and Co. (1921).
2) E. Moses, J. Campbell, C. Stolz, C. Wuest, SPIE 5001 (2003) 1.
3) M. Feit, A. Rubenchik, "Influence of subsurface cracks on laser induced surface damage", SPIE 5273 (2003) 264-272.
4) T. Izumitani, Optical Glass (American Institute of Physics, New York, 1986).
5) H. Karow, "Fabrication Methods for Precision Optics" John Wiley & Sons (1993).
6) N. Brown, "Optical Fabrication", Lawrence Livermore National Laboratory Report , MISC 4476, August 1989.
7) B. Lawn, "Fracture of Brittle Solids- Second Edition" Cambridge Solid State Science Series (1993)
8) B. Lawn, R. Wilshaw, "Indentation fracture: principles and applications", Journal of Materials Science, 18 (1975) 1049-1081.
9) I. Hutchings, "Tribology: Friction and Wear of Engineering Materials", Butterworth/ Heinmann (1992).
10) B. Bhushan, "Introduction to Tribology", John Wiley & Sons (2002).
11) M. Chaudhri, J. Mat. Sci. 15 (1980) 345.

12) J. Lambropoulos, T. Fang, P. Funkenbusch, S. Jacobs, M. Cumbo, D. Golini, "Surface microroughness of optical glasses under deterministic microgrinding" Applied Optics 35(22) (1996) 4448-4462.

13) F. Aleinkov, "The effect of certain physical and mechanical properties on the grinding of brittle materials", Sov. Phys. Tech. Phys. 27 2529 (1957).

14) F. Preston, "Structure of abraded surface glasses", Trans. Opt. Soc. 23(3) 141-162 (1922).

15) E. Brinksmeier, "State-of-the-art non-destructive measurement of subsurface material properties and damages", Precis. Eng. 11 (1989) 211-224.

16) D. Lucca, W. Brinksmeier, G. Goch, "Progress in Assessing Surface and Subsurface Integrity" Annuals of the CIRP 47(2) (1998) 669-693.

17) R. Parks, "Sub-surface damage in Optically Worked Glasses", American Society of Precesion Engineering (1989) 1.

18) T. Magee, C. Leung, "Overview of sub-surface damage in Brittle Materials", American Society of Precision Engineering (1989)

19) J. Lambropoulos, Y. Li, P. Funkenbusch, and J. Ruckman, SPIE 3782(1999) 41.

20) Y. Zhou, P. Funkenbusch, D. Quesnel, D. Golini, and A. Lindquist, "Effect of etching and imaging mode on the measurement of subsurface damage in microground optical glasses" J. Amer. Ceram. Soc. 77 (1994) 3277-3280.

21) P. Hed, D. Edwards "Optical glass fabrication technology. Relationship between surface roughness and subsurface damage", Applied Optics 26:21 (1987) 4677.

22) J. Randi, J. Lambropoulos, S. Jacobs, "Subsurface damage in some single crystalline optical materials" Applied Optics 44(12) (2005) 2241-2249.

23) J. Menapace, P. Davis, L. Wong, W. Steele, T. Suratwala, P. Miller, "Measurement of Process-dependent subsurface damage in Optical Materials using the MRF technique" SPIE 5991, Boulder Damage Symposium XXXVII (2005).

24) P. Miller, T. Suratwala, L. Wong, M. Feit, J. Menapace, P. Davis, R. Steele, "The distribution of subsurface damage in fused silica", SPIE 5991, Boulder Damage Symposium XXXVII (2005).

25) B. Lawn, "Partial cone crack formation in a brittle material loaded with a sliding spherical indenter", Proceedings of the Royal Society, Series A, Mathematical and Physical Sciences, 299(1458) (1967) 307.

26) L. Cook, "Chemical processes in glass polishing", J. Non-Cryst. Solids 120 (1990) 152-171.

27) V. Bulsara, Y. Ahn, S. Chandrasekar, T. Farris, "Mechanics of Polishing", Transctions of the ASME, 65 (1998) 410.

28) R. Chauhan, Y. Ahn, S. Chandrasekar, T. Farris, "Role of indentation fracture in free abrasive machining of ceramics", Wear (162) 246.

29) M. Bennett, L. Mattson, "Introduction to surface roughness and scattering", Optical Society of America, Washington D.C. (1993).

30) J. Lambropoulos, "Subsurface damage in microgrinding optical glasses", LLE Review: Quarterly Report 73 (Oct-Dec 1997) 45.

Definition of Terms

χ_h = Hertzian crack depth growth constant (unitless)

χ_ℓ = lateral crack depth growth constant (unitless)

χ_r = radial crack depth growth constant (unitless)

$<c>$ = mean crack depth (m)

$<d>$ = mean particle size causing surface fracture (m)

$<L>$ = mean crack length (m)

A = Auerbach's constant for initiation of Hertzian fracture (N/m)

a = contact zone radius for a Hertzian indent (m)

B = Friction effect constant for trailing indent fracture (unitless)

c_h = Hertzian crack depth (m)

c_ℓ = lateral crack depth (m)

c_{max} = maximum crack depth (m)

c_r = Radial crack depth (m)

c_t = Trailing Indent crack depth (m)

d = abrasive particle size (m)

d_c = mean abrasive particle size (m)

d_c = mean particle size of abrasive used during polishing

d_{max} = maximum particle size causing surface cracking (m)

d_{optic} = diameter of optic/workpiece (m)

E = Young's modulus of optic/workpiece (GPa)

E_p = Young's modulus of abrasive particle (GPa)

f = Fill fraction of particles between lap and workpiece

$F_c(c)$ = cumulative distribution of crack depths

$f_c(c)$ = fractional distribution of crack depths

$F_d(d)$ = cumulative distribution of particle sizes participating in causing surface cracking

$f_d(d)$ = fractional distribution of particle sizes participate in causing surface cracking

$F_L(L)$ = cumulative distribution of crack lengths

$f_L(L)$ = fractional distribution of crack lengths

$f_{load}(c)$ = fraction of particles being loaded for various crack depths (unitless)

$f_o(c)$ = instantaneous fractional distribution of crack depths created

i = number of increments of material removal (unitless)

k	=	material constant for Poisson's ratio and modulus of indentor and substrate (unitless)
K_{Ic}	=	fracture toughness of optic/workpiece (MPa m$^{1/2}$)
K_{Ic}	=	fracture toughness of fused silica
k_{max}	=	proportionality constant between c_{max} and δ
L	=	crack length (m)
L_{max}	=	maximum crack length (m)
L_t	=	length of a trailing Indent crack (m0
n	=	number density of cracks at the surface (cm^{-2})
N_L	=	number of abrasive particles being loaded
N_T	=	total number of particle between workpiece/optic and lap
O(c)	=	cumulative obscuration of cracks
o(c)	=	fractional obscuration of cracks
P	=	normal load (N)
P_{ch}	=	fracture initiation load for Hertzian cone crack (N)
$P_{c\ell}$	=	fracture initiation load for lateral crack (N)
P_{cr}	=	fracture initiation load for radial crack (N)
P_{ct}	=	fracture initiation load for trailing Indent crack (N)
P_{max}	=	load/particle that leads to the maximum SSD (N)
P_T	=	total load on sample (N)
r	=	radius of curvature for Indent indenter (m)
s	=	shape factor relating the radius of curvature of contact of the particle with the vertical dimension of the particle
t	=	time of grinding or polishing (sec)
w	=	crack width (m)
z	=	coordinate describing amount of material removed during grinding/polishing (m)
z_w	=	wedge depth (m)
Δ	=	surface material removal increment (m)
Ω	=	Proportionality constant between crack length and depth (unitless)
α_r	=	fracture initiation constant for radial cracks (unitless)
ν	=	Poisson's ratio of optic/workpiece (unitless)
ν_p	=	Poisson's ratio of abrasive particle (unitless)

Table 1: Summary of data and model parameters for fused silica samples A-L.

Description	Variable	A	B	C	D	E	F	G	H	I	J	K	L
Sample		Sandblast	120 grit Generator	150 grit Generator	15 μm Loose abrasive	15 μm Fixed Abrasive	9 μm Loose Abrasive	7 μm Fixed Abrasive	9 μm Loose Abrasive (220 N)	9 μm Loose Abrasive (580 N)	9 μm + 0.1 wt% 15 μm loose abrasive	120 / 150 grit Generator	120 / 150 grit Generator (etch)
Process Parameters													
Abrasive Size (μm)	d_c	300	125	100	15	15	9	7	9	9	9	100	100
Pressure (psi)	ρ	nm	nm	nm	0.4	0.4	0.4	0.4	4.0	10.4	0.4	nm	nm
Rotation Rate (rpm)	r	na	45	41	16	16	16	16	16	16	16	45/ 41	45/ 41
Measured Values													
Wedge depth (μm)	z_w	108	77	49	34	40	31	18	43	52	51	41	50
SSD depth (μm)	c_{max}	131	79	42	31	18	6	28	25	42	47	44	47
Weighted surface roughness (n=4) (μm)	δ	16.1	1.88	0.63	0.63	0.29	0.36	0.27	nm	nm	nm	nm	nm
Peak-to-valley surface roughness(μm)	δ_{PV}	38.2	8.55	3.19	3.69	0.76	1.39	1.44	nm	nm	nm	nm	nm
Mean crack length (μm)	$<L>$	27	28	15	4.6	4.5	2.0	8.4	7.0 / 3.3	3.8/ 18.3	3.7/ 10	19	18
Maximum load per particle (N)	P_{max}	33	15.3	6	3.7	1.7	0.33	3.4	2.8	6	7.3	6.4	7.1
Pre-exponent for F(L)	A	0.83	0.94	1.01	1.31	1.65	1.23	0.83	0.84 /0.86	1.74/ 0.1	0.72/ 0.81	1.01	1.02
Maximum crack length (μm)	L_{max}	384	174	94	48	28	12	218	30	62	70	175	130
Crack Width (μm)	w	8.1	5.9	4.4	4.4	4.4	1.5	4.4	5.2	5.2	5.2	4.2	4.1
Fitting Parameters													
Load / particle (Newton)	P_T/N_L	0.14	0.05	0.01	0.005	0.003	$8 \cdot 10^{-5}$	$6 \cdot 10^{-4}$	$1.6 \cdot 10^{-4}$ / 0.14	$1 \cdot 10^{-3}$ / 0.41	$6.9 \cdot 10^{-3}$ / 0.1	$1 \cdot 10^{-2}$	$1 \cdot 10^{-2}$
Surface density of cracks (10^5 cm^{-2})	n	2.5	5	15	10	40	$3 \cdot 10^{10}$	8	$4.5 \cdot 10^4$/ 0.09	$3 \cdot 10^7$/ 0.03	$1 \cdot 10^4$/ 0.012	15	15
Maximum crack length (μm)	L_{max}	nm	234	183	nm	68	68	nm	23	26	47	205	220
Calculated Model Parameters													
Mean effective particle (μm)	$<d>$	1380	1500	1000	115	140	206	536	900 / 10	147 / 76	54 / 64	1660	1550
	Ω	2.9	3.0	4.4	3.2	3.8	10.7	5	8.6 / 0.9	4.7 / 0.6	2.4 / 1.0	4.8	4.8
Mean crack depth (μm)	$<c>$	9	9.3	3.4	1.4	1.2	0.17	1.7	na	na	na	4.0	3.8
Fraction of Particles Loaded	F_L at c_{max}	na	na	na	5×10^{-7}	1×10^{-6}	2×10^{-6}	1×10^{-7}	2×10^{-6}	3×10^{-6}	9×10^{-8}	na	na

na = not applicable; nm = not measured

Table 2: Crack dimensions from blunt and sharp indent as a function of load

| | Hertzian (Blunt) | | | | Vickers (Sharp) | | |
| | Cone | | | | Lateral | Radial | |
Load (N)	s (µm)	2a (µm)	d (µm)	c_h (µm)	c_{t1} (µm)	2a (µm)	c_r (µm)
0.10					*	2.2	2.2
0.25					*	4.2	4.2
0.49					*	5.7	6.3
0.98					*	8.0	8.8
2.0					2	11.3	13.6
2.9					2	13.1	24.2
4.9					5	17.1	35.3
9.8					10	24.0	52.8
10	*	*	*	*			
20	170	130	10.2	22	15	30.3	70.4
39	220	140	24.8	47			
59	420	160	52.6	140			
98	490	160	58.4	175			
120	620	170	87.6	241			

* indentation made, but no crack initiation observed

Table 3: Measured Indentation parameters for Fused Silica

Indentation parameters	Variable	Value (this study)	Literature value
Initiation constant for Hertzian cracks (Auerbach's constant)	A	$3.0 \cdot 10^4$ N/m	$9 \cdot 10^4$ N/m [2]
Growth constant for Hertzian cracks	χ_h	0.034	0.03 [2]
Initiation constant for radial cracks	α_r	$3.5 \cdot 10^5$	$1.4 \cdot 10^4$ [2]
Growth for radial cracks	χ_r	0.024	0.0186 [8]
Initiation constant for lateral cracks	$P_{c\ell}$	1.5 N	Not found
Growth depth constant of lateral cracks	$\chi_{\ell 1}$	0.13	Not found
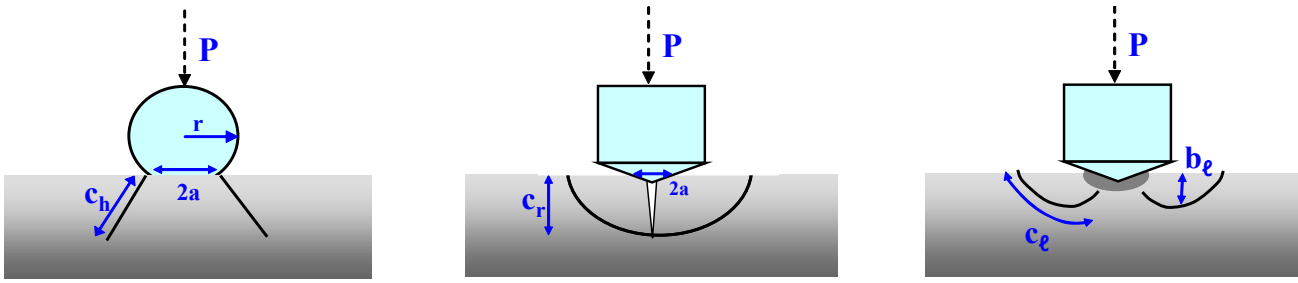
Figure 1. Schematic illustration of the fracture geometry of the idealized fractures created by static indentation; (a) Hertzian cone crack from a blunt indenter, (b) radial or median cracks from a sharp indenter, (c) lateral crack from a sharp indenter
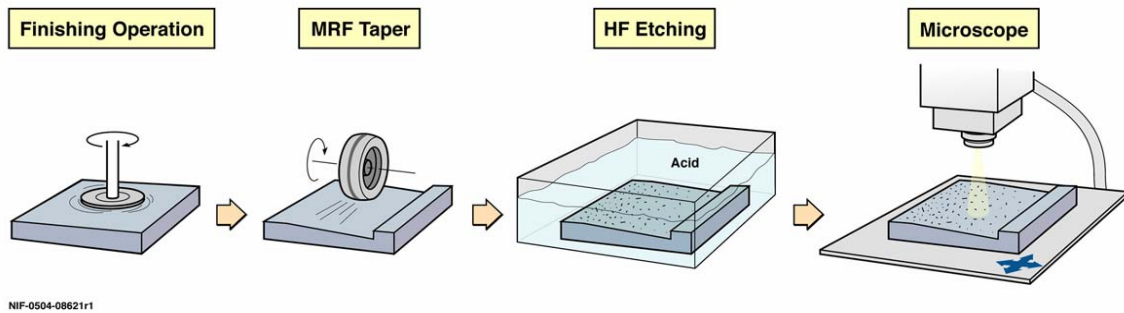
Figure 2: Schematic illustrating the step in the wedge technique to determine the SSD depth distribution.
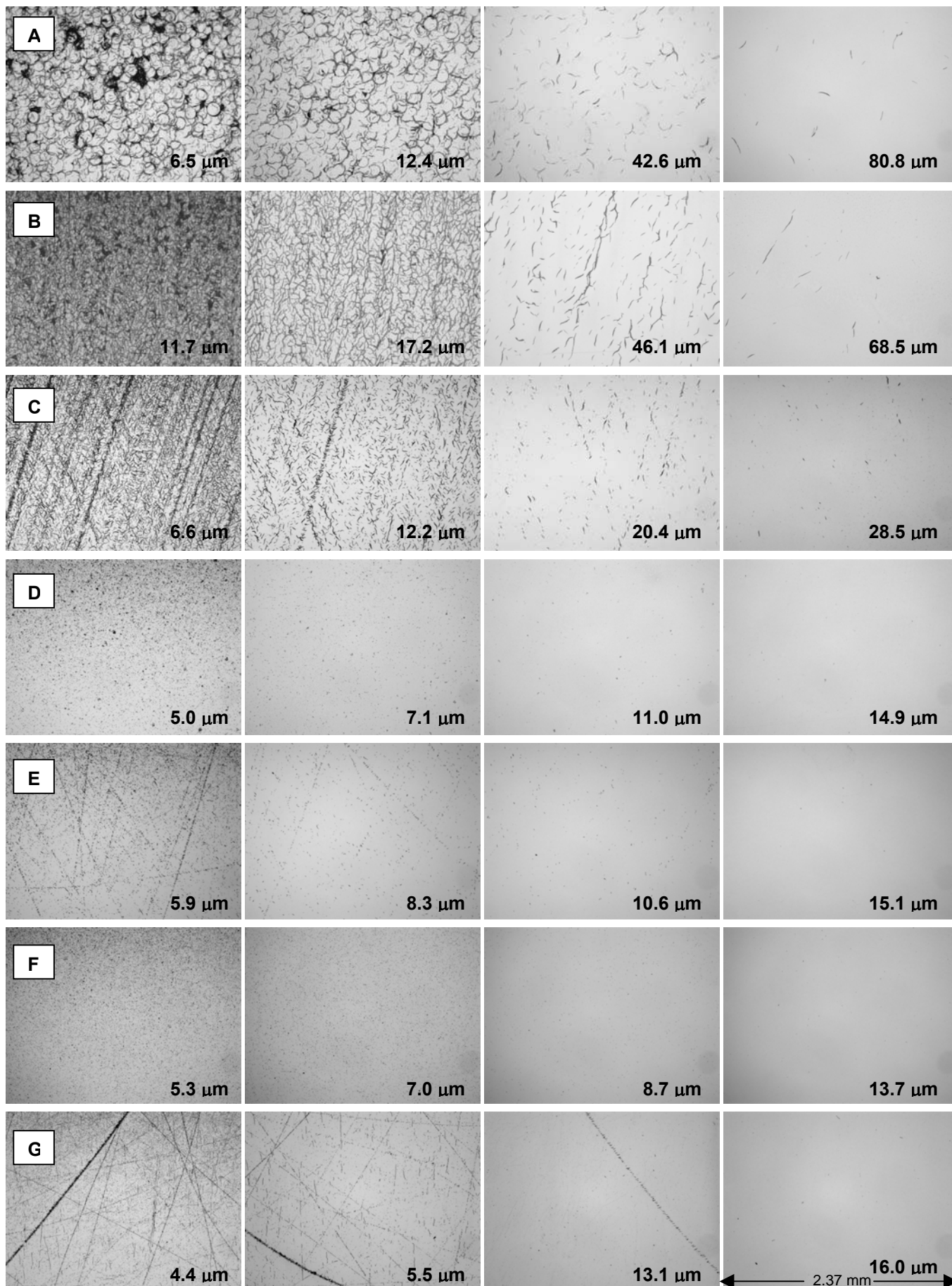
Figure 3: Optical microscopy images for fused silica surfaces that have been treated by a wide variety of grinding processes (Samples A-G). The images for each sample are at various depths of removal using the wedge technique. The value in the bottom right is the depth below the original surface at which the image was taken.
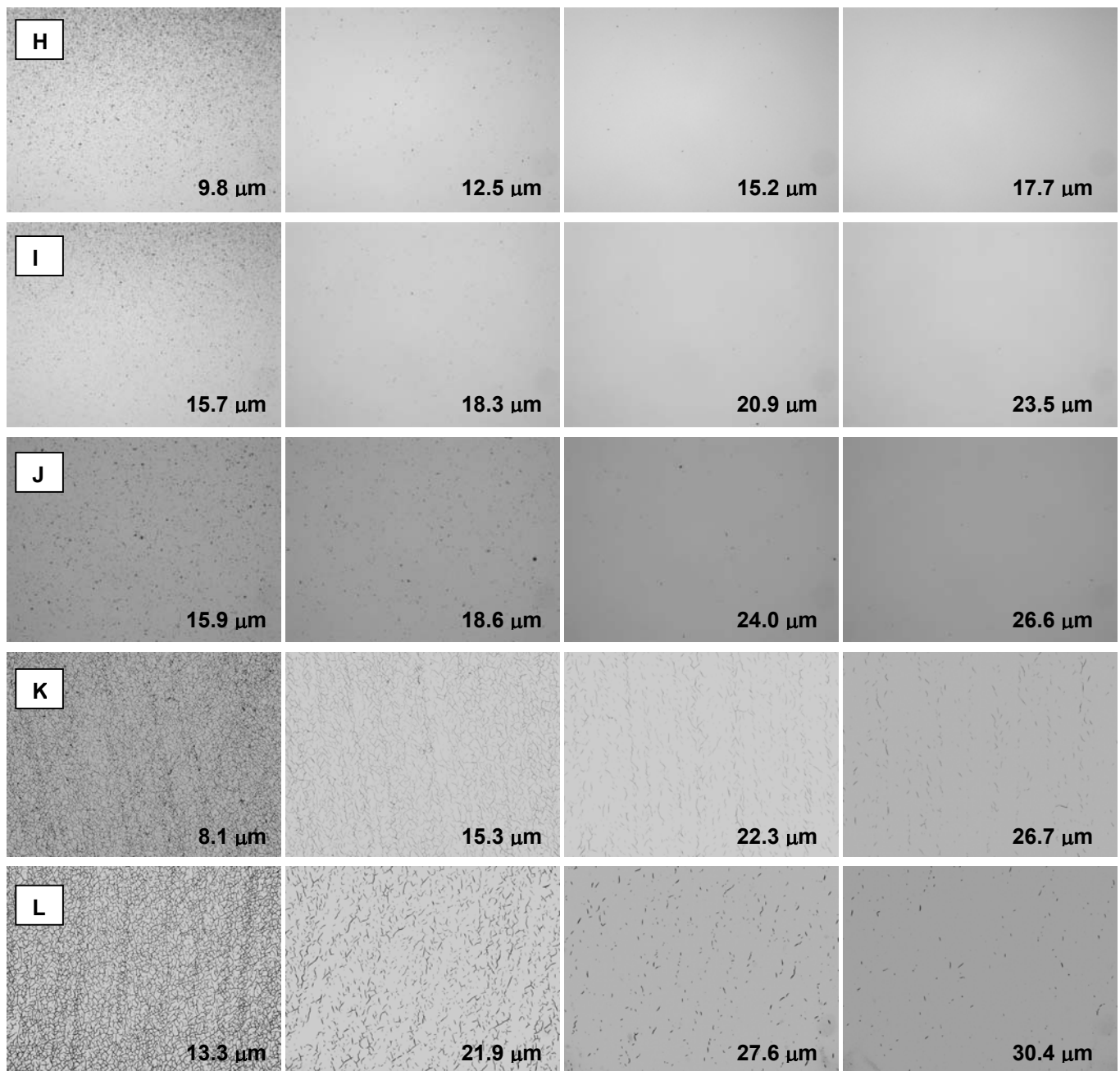
Figure 4: Optical microscopy images for fused silica surfaces that have been treated by a range of grinding processes using the wedge technique (Samples H-L). The value in the bottom right is the depth below the original surface at which the image was taken.
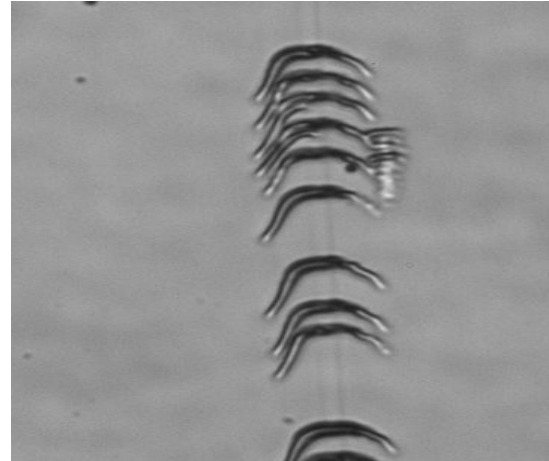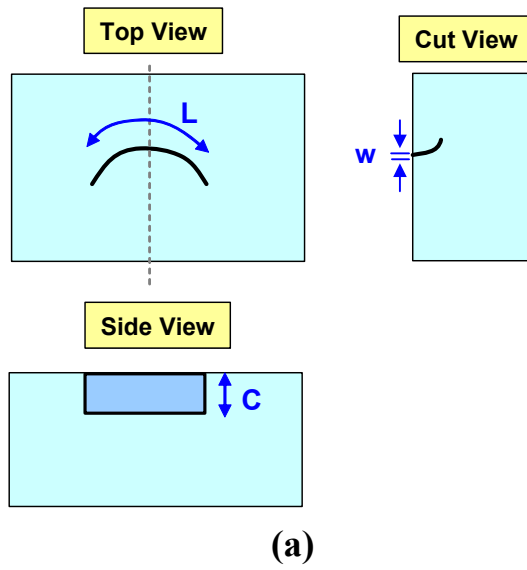
Figure 5. (a) Proposed geometry and nomenclature for dimensions of an individual trailing indent fracture, (b) Optical micrograph of a trailing indent crack in a fine scratch that has been BOE etched (the crack length is ~10 μm).
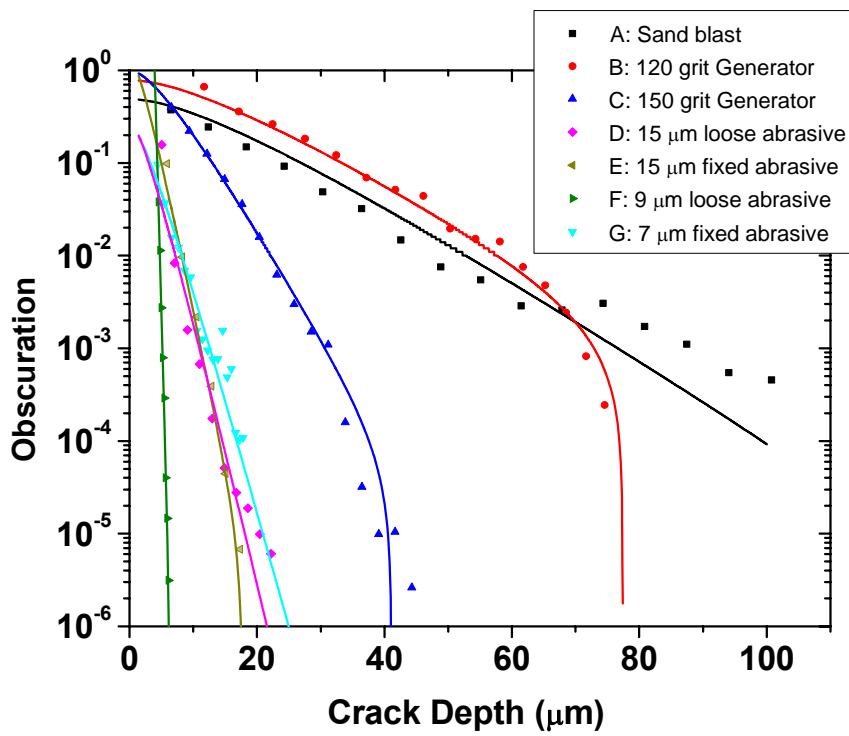
(a)
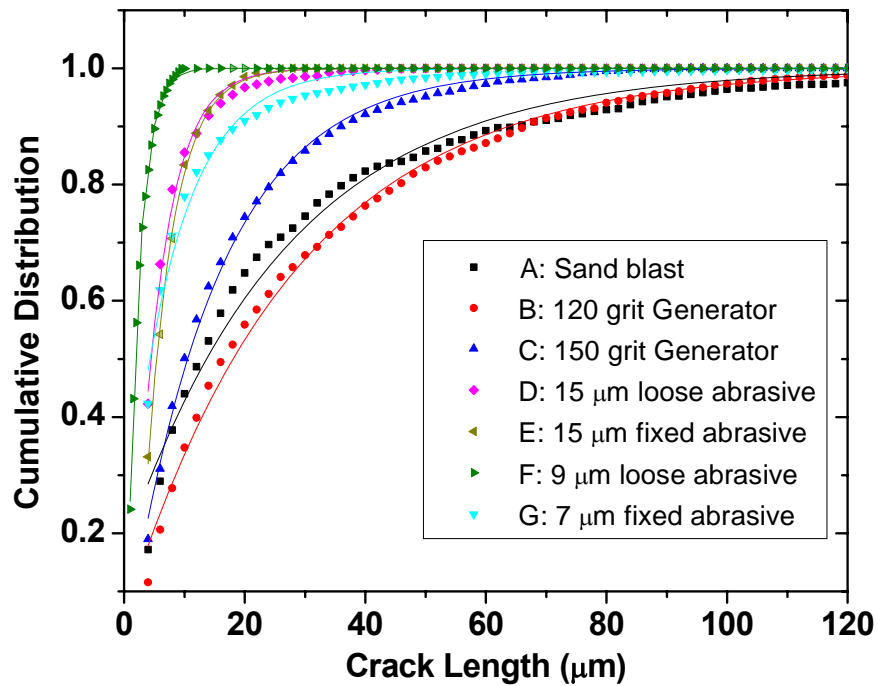
(b)

Figure 6: (a) Measured cumulative crack depth distributions for fused silica surfaces that have been treated by a wide variety of grinding processes (Samples A-G). The plots are semi-log plots as crack obscuration versus crack depth. (b) Measured cumulative crack length distributions for Samples A-G. The points represent data points and the lines represent best fits to the data using Eq. 18.
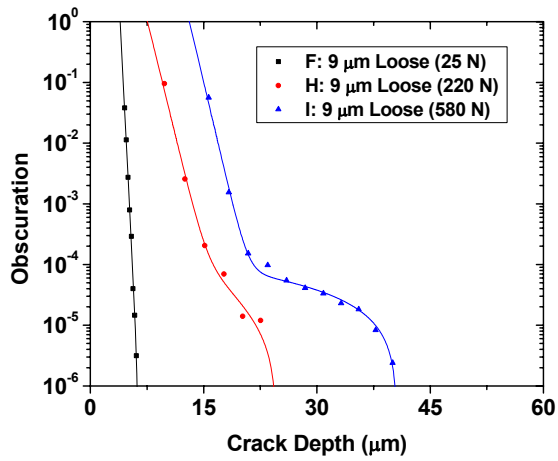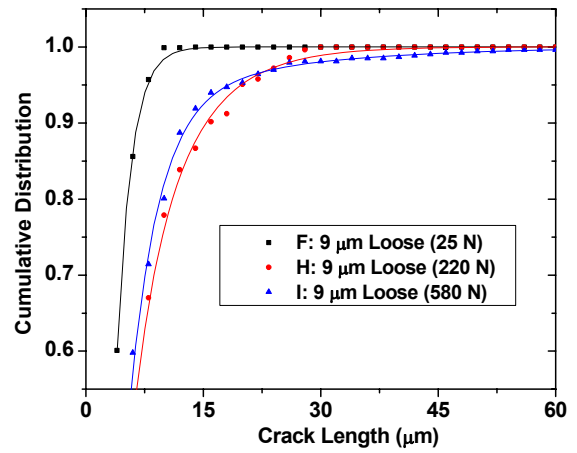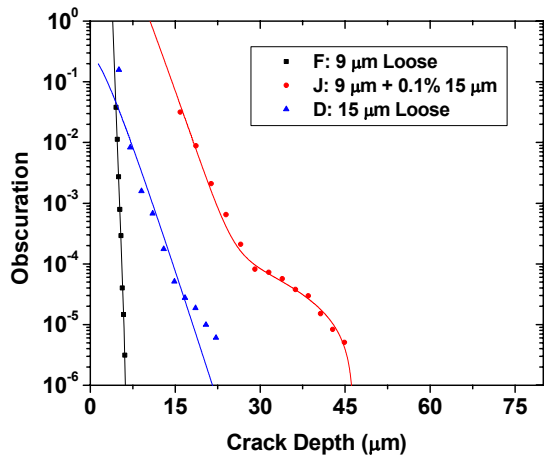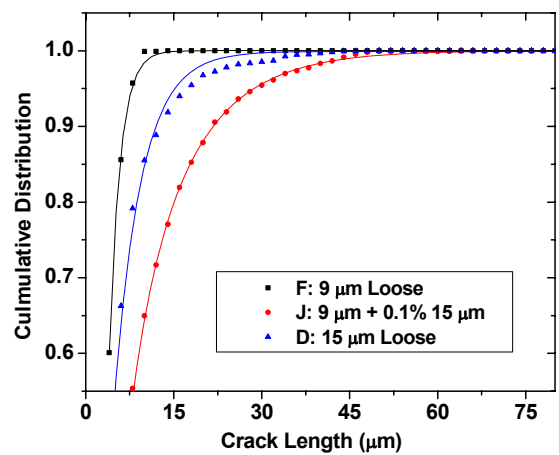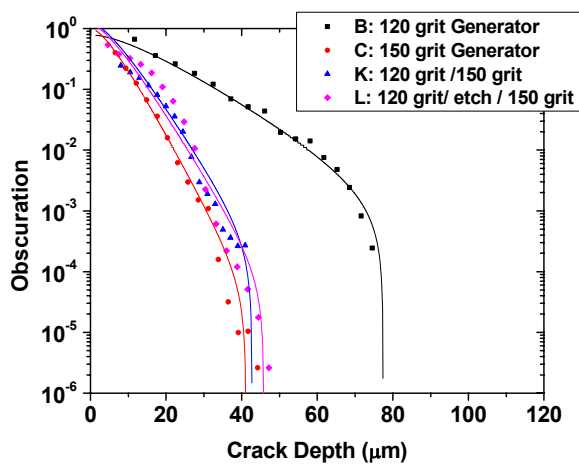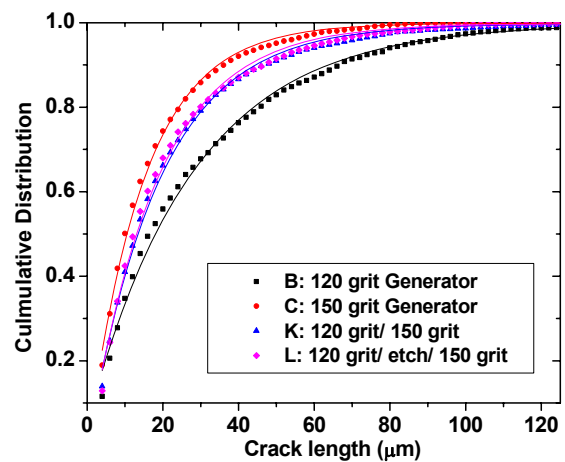
Figure 7: Measured cumulative crack depth distributions for fused silica surfaces (a) as a function of load (b) with particle contamination (c) with grinding steps performed in series. The plots are semi-log plots as crack obscuration vs crack depth. (d-f) Measured cumulative crack length distributions for the same samples listed in a-c. The points represent data points and the lines represent best fits to the data using Eq. 18.
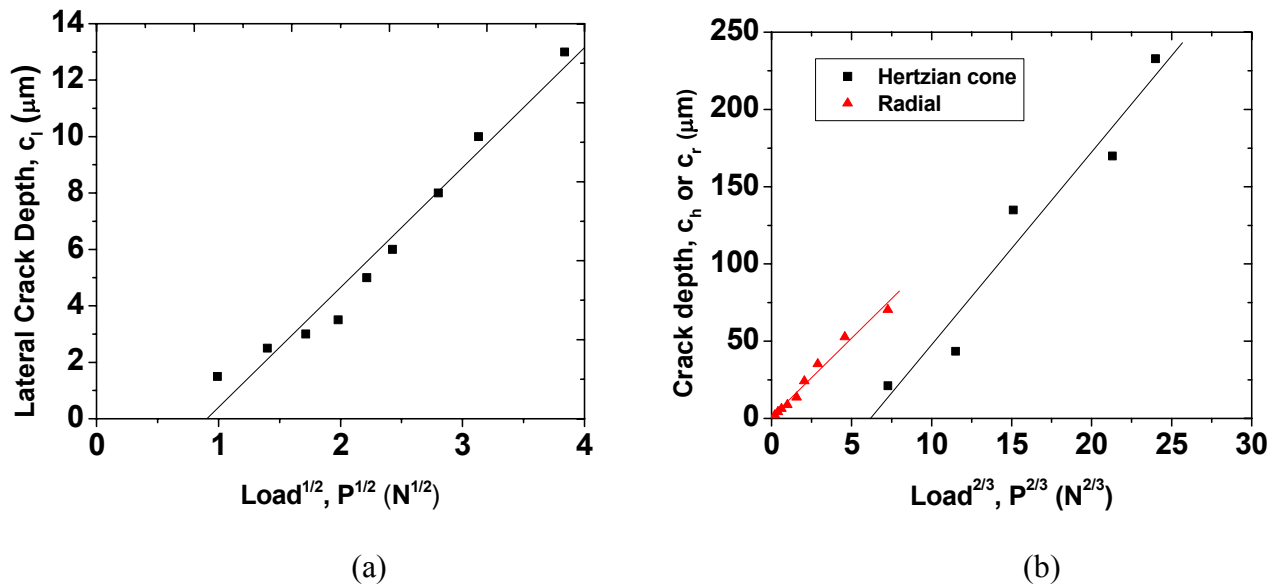
Figure 8: (a) Lateral crack depth as a function of load $^{1/2}$ to determine $\chi_{\ell 1}$; (b) Hertzian cone depth and radial crack depth as a function of load $^{2/3}$ to determine χ_h and χ_r. The lines represent the best linear fits to the data.
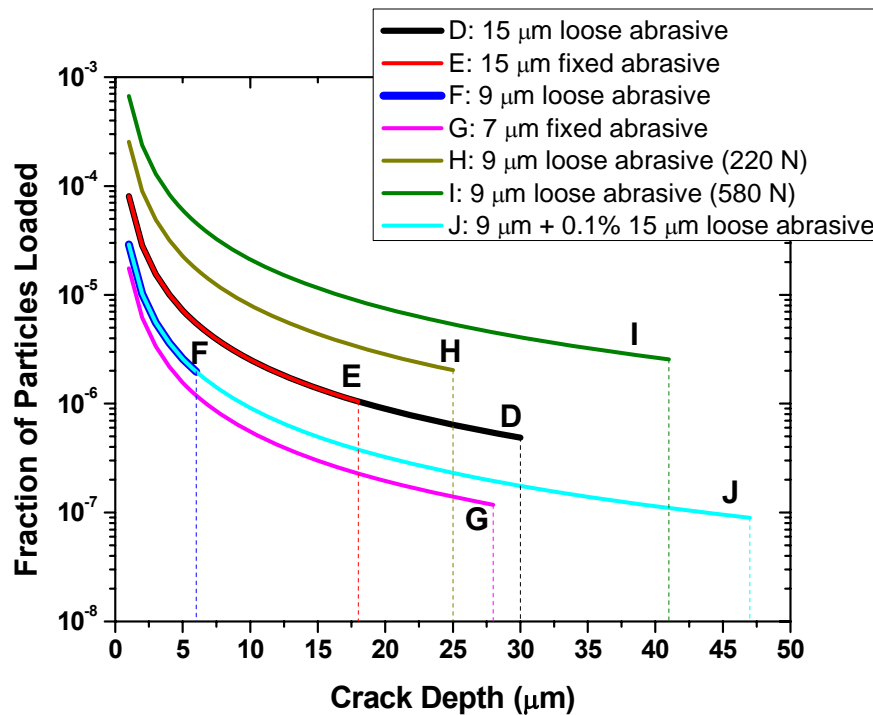
Figure 9: Calculated fraction of the total particles below the workpiece being loaded as a function of the depth of the crack assuming that only one type of crack is created at one instance. The values were determined using Eq. 5.
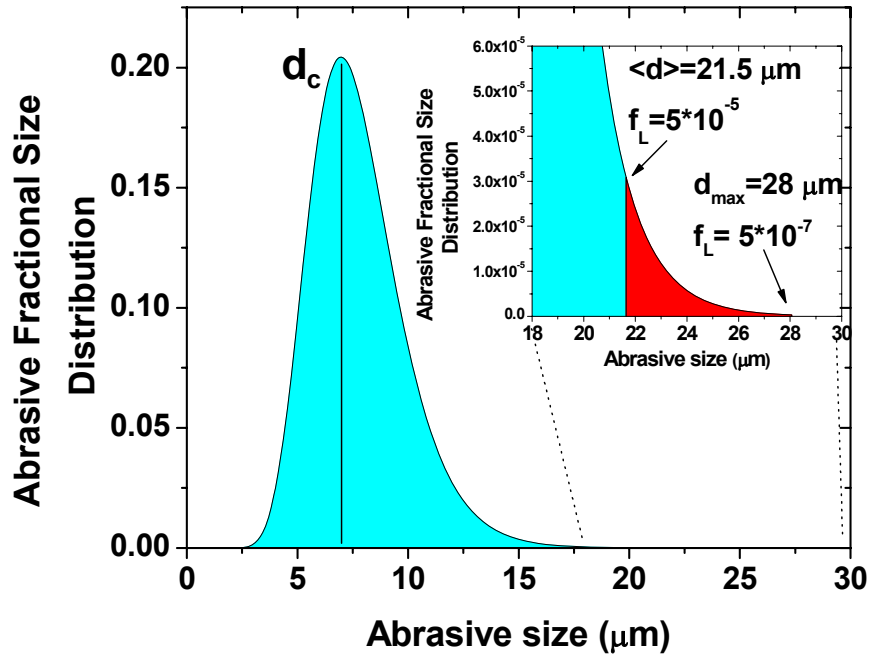
Figure 10. Abrasive fractional size distribution and the estimated range of particles being loaded and used to cause fracture.

(a)

(b)

(c)
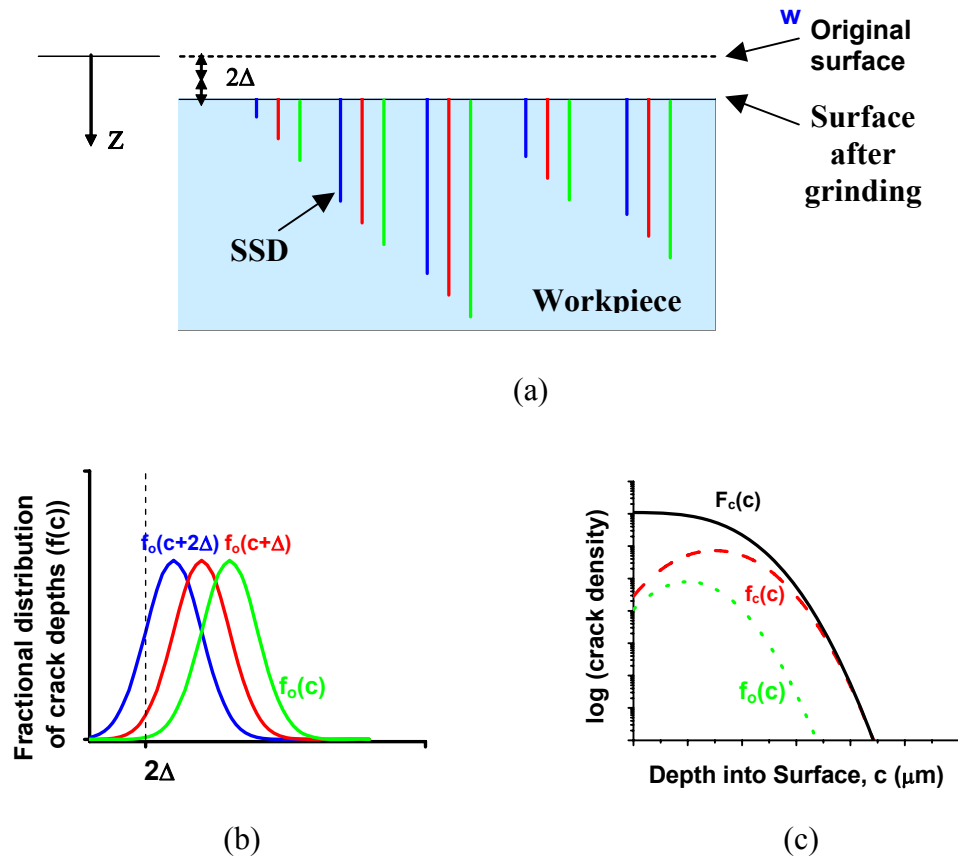
Figure 11: (a) Schematic illustration of the creation and removal of cracks as a function of surface removal; (b) schematic illustration instantaneous distribution of crack depths ($f_o(c)$) for different removal increments of Δ;(c) schematic illustration comparing $f_o(c)$, $f_c(c)$ and $F_c(c)$ (see Eqs. 6 & 7) on a semilog plot.
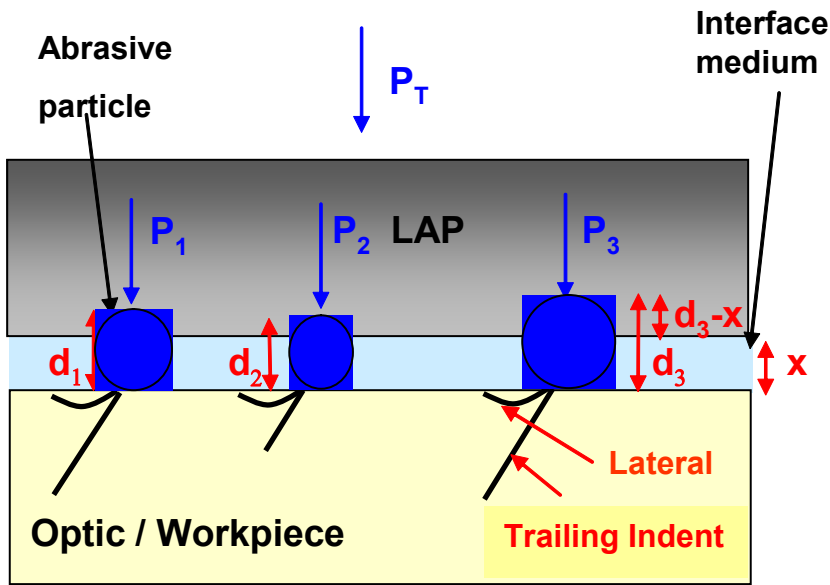
26

Figure 12: Schematic of the working model to describe the development of SSD during grinding
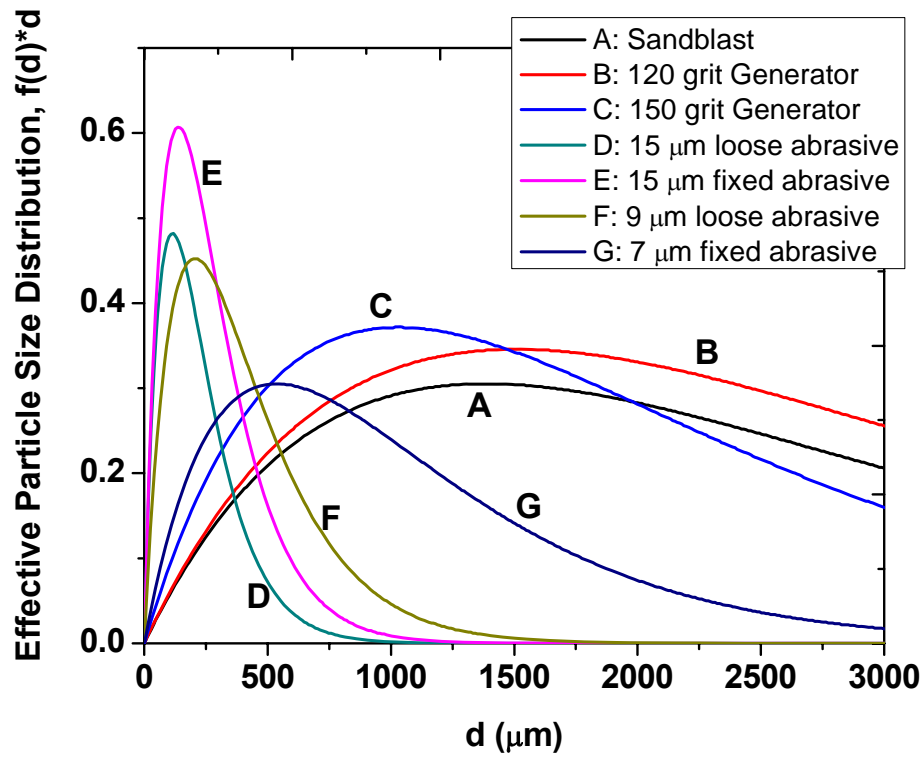

Figure 13. Calculated 'effective' particle size distributions participating in the surface fractures using the measured crack length distributions for Samples A-G and Eq 20a & b.
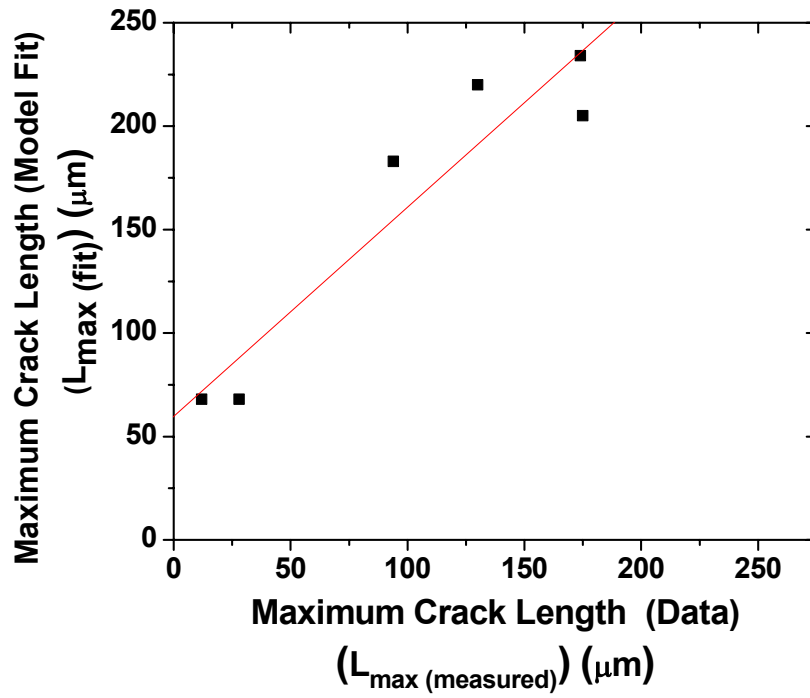
Figure 14: Correlation between the measured maximum crack length (L_{max}(measured) and the best fit L_{max} determine by fitting the crack depth distributions to Eq. 18. (Note not all the samples had a L_{max} that could be fit to data; hence data for those samples are not included.)
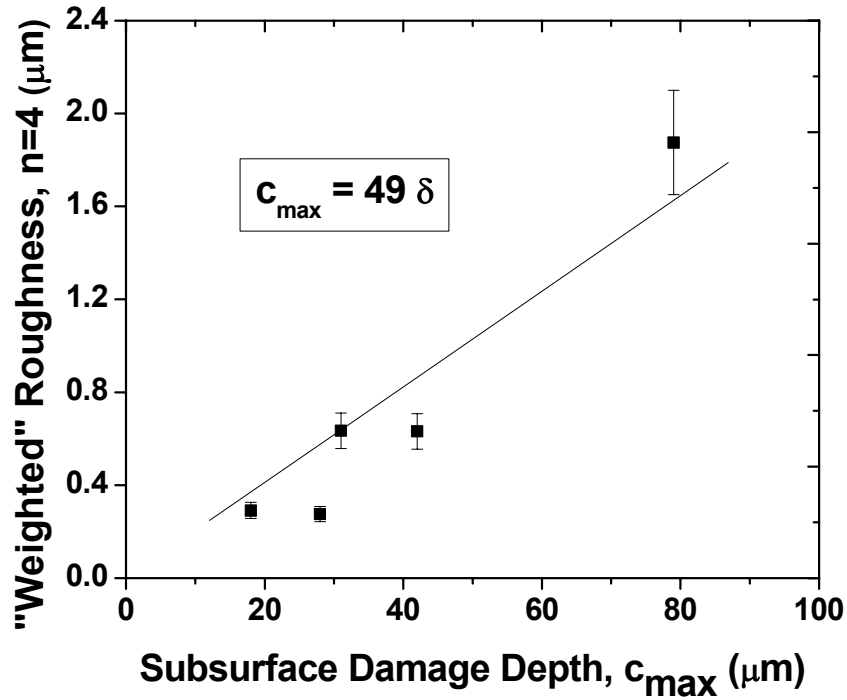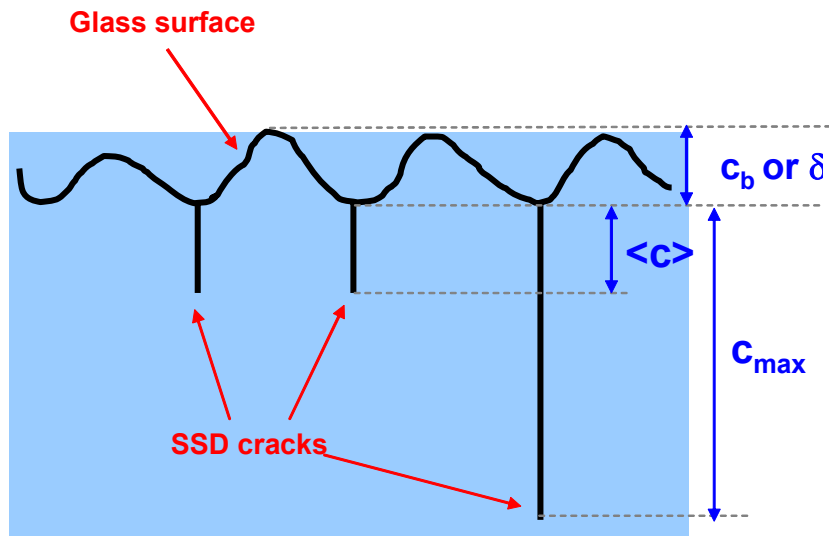
(a)
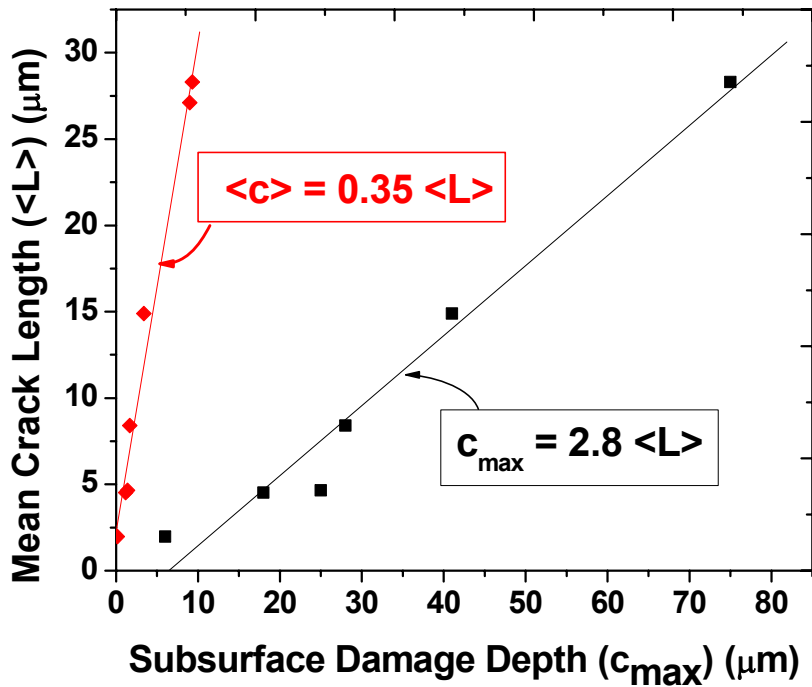
(b)

Figure 15: (a) Correlation of the maximum SSD depth (c_{max}) with surface roughness. (b) Correlation of maximum SSD depth (c_{max}) and the average SSD depth ($<c>$) with the measured mean crack length ($<L>$).

Figure 16. Illustration between SSD depth and surface roughness.